



# From Real Artifacts to Virtual Reference: A Robust Framework for Translating Endoscopic Images

Junyang Wu<sup>a</sup>, Fangfang Xie<sup>b</sup>, Jiayuan Sun<sup>b</sup>, Yun Gu<sup>a</sup>, Guang-Zhong Yang<sup>a</sup>

<sup>a</sup>*Institute of Medical Robotics, Shanghai Jiao Tong University, Shanghai, CHINA.*

<sup>b</sup>*Shanghai Chest Hospital, Shanghai, CHINA*

## ARTICLE INFO

### Article history:

Received 1 May 2013

Received in final form 10 May 2013

Accepted 13 May 2013

Available online 15 May 2013

**Keywords:** Image translation, Endoscopic images, Robustness

## ABSTRACT

Domain adaptation, which bridges the distributions across different modalities, plays a crucial role in multimodal medical image analysis. In endoscopic imaging, combining pre-operative data with intra-operative imaging is important for surgical planning and navigation. However, existing domain adaptation methods are hampered by distribution shift caused by *in vivo* artifacts, necessitating robust techniques for aligning noisy and artifact abundant patient endoscopic videos with clean virtual images reconstructed from pre-operative tomographic data for pose estimation during intraoperative guidance. This paper presents an artifact-resilient image translation method and an associated benchmark for this purpose. The method incorporates a novel “local-global” translation framework and a noise-resilient feature extraction strategy. For the former, it decouples the image translation process into a local step for feature denoising, and a global step for global style transfer. For feature extraction, a new contrastive learning strategy is proposed, which can extract noise-resilient features for establishing robust correspondence across domains. Detailed validation on both public and in-house clinical datasets has been conducted, demonstrating significantly improved performance compared to the current state-of-the-art.

© 2024 Elsevier B. V. All rights reserved.

## 1. Introduction

Inspired by the success of autonomous driving, pure vision-based techniques for intra-operative guidance are gaining increasing clinical interests, as they eliminate the need of additional electromagnetic or optical tracking instruments and facilitate further miniaturization of endoscopic devices for reaching narrow, distal lumina. In endoluminal intervention, an essential application is to combine preoperative imaging such as CT with intra-operative endoscopic images for position and pose estimation. Under this scenario, preoperative multi-slice CT or MRI is used to reconstruct a 3D virtual scene for surgical planning and intra-operative guidance. This is achieved by co-registering real-time 2D endoscopic videos with the 3D map, enabling the accurate recovery of the instrument tip’s position and orienta-

tion while accounting for physiological motion and tissue deformation. However, significant challenges arise when aligning these two imaging domains due to artifacts such as fluid, bleeding, motion blur and foreign objects, further exacerbated by a lack of distinctive surface textures or anatomical landmarks for co-registration.

To address this challenge, deep learning-based approaches, particularly those based on domain adaptation, have made notable progresses in recent years. Existing methods focus on either feature-level domain adaptation (Tzeng et al., 2017; Ganin et al., 2016; Vu et al., 2019; Wang et al., 2019; Luo et al., 2019; Lee et al., 2019; Tsai et al., 2018) or image-level domain adaptation (Zhu et al., 2017; Park et al., 2020; Zhao et al., 2020; Zhao and Chen, 2021; Razavi et al., 2019; Tiwary et al., 2024;

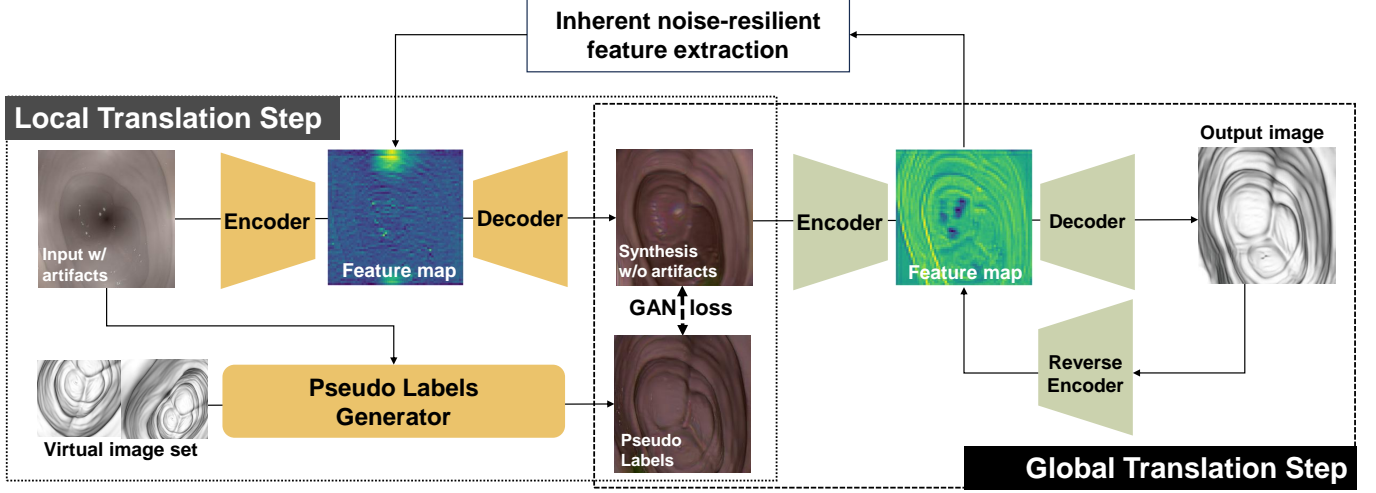


**Fig. 1.** Overview of the proposed method for transferring from images with artifacts to clean virtual image. The transfer step is divided into two steps. In the local translation step, a pseudo-labels generator produces real images without artifacts. These images are used as labels to train the local network, enabling it to generate images without artifacts. In the global translation step, the global network transfers the whole style from real domain to the virtual domain. Inherent resilient feature extractor extracts inherent stable features from virtual images, guiding the local network in extracting noise-resistant features.

Ho et al., 2020; Sasaki et al., 2021; Zhao et al., 2022a; Kim et al., 2023). Feature-level domain adaptation involves mapping images from different modalities to a shared latent space to extract domain-invariant features for downstream analysis tasks, whereas image-level domain adaptation, known as image translation, transfers data from a given source domain to the target domain. This method captures the distributions of both domains at the latent feature level and employs learning-based techniques such as Generative Adversarial Networks (GANs) (Zhu et al., 2017; Park et al., 2020; Tang et al., 2021; Mathew et al., 2020), energy-based methods (EBMs) (Zhao et al., 2020; Zhao and Chen, 2021; Razavi et al., 2019; Tiwary et al., 2024), and diffusion-based models (Ho et al., 2020; Sasaki et al., 2021; Zhao et al., 2022a; Kim et al., 2023) to bridge different domains effectively.

In Generative Adversarial Networks (GANs), a generator generates target-like images from the source domain images, while a discriminator measures the similarity between the generated domain and the target domain. As the iterative learning progresses, the generator can create target domain images that cannot be distinguished by the discriminator. Different attempts have been made to refine different GAN architectures like CycleGAN (Zhu et al., 2017) and CUT (Park et al., 2020). CycleGAN introduced the concept of cycle-consistency loss, enabling unpaired image translation. Furthermore, CUT introduced a contrastive learning approach, which relaxed the necessity of a one-to-one mapping between the source and target domains in GANs by maximizing the mutual information between corresponding input and output patches. Energy-based models (EBMs), unlike GANs, directly model a probability distribution over the data. They learn an energy function that assigns lower energy to plausible images and higher energy to implausible ones. For instance, CF-EBM (Zhao et al., 2020) applied

Langevin Dynamics as the guidance to map the source image feature to the lower energy direction. LETIT (Zhao and Chen, 2021) proposed a more efficient methods using the low dimensional latent features produced by VQ-VAE2 (Razavi et al., 2019) to address the slow convergence issue observed in CF-EBM. Moreover, CCT-EBM (Tiwary et al., 2024) proposed a twin network containing a pair of EBMs in the feature space to improve the structure consistency. Diffusion-based models, which can iteratively denoise images through a reverse diffusion, also exhibit the capability to generate high-quality target images (Ho et al., 2020; Sasaki et al., 2021; Zhao et al., 2022a; Kim et al., 2023).

In real surgical scenarios, however, translating endoscopic images can be difficult due to unpredictable artifacts such as blood, mucus, and bubbles. These unpredictable artifacts make it difficult to directly map virtual images to real scenes. To address this problem, this study focuses on transferring artifact-affected real images to virtual 3D scenes reconstructed from pre-operative CT data. This process can be seen as a combination of artifact removal and image translation. The main processing flow and the rationale of the proposed method is illustrated in Figure 1, which features two main components: a “local-global” translation framework and a noise-resilient feature extraction strategy.

**“Local-global” translation framework:** Due to the intricate artifacts in noise-containing input images, a single image translation network is insufficient to directly map them into the virtual domain. This study decouples the translation procedure into two stages: a local translation step and a global translation step. During the first step, a local GAN concentrates on debiasing the distribution shifts caused by artifacts. In the second step, a global GAN transfers the overall style from the real domain to the virtual domain.

**Noise-resilient feature extraction:** Another key challenge in robust image translation is extracting robust features from noisy images. To overcome this obstacle, this study proposes a novel contrastive learning strategy. It leverages the inherent noise-resilient features from the virtual domain as a reference to guide the extraction of features from noisy images.

Overall, the main contribution of this paper includes the following:

- A new benchmark is proposed to evaluate the robustness of image translation models, providing a comprehensive analysis of their performance under both synthetic and real-world artifacts, and thoroughly discussing the bottleneck.
- A two-stage framework is developed for artifact-resilient image translation, where a local GAN mitigates distribution shifts caused by artifacts, and a global GAN performs global style transfer from the real domain to the virtual domain.
- A novel contrastive learning strategy is established, which leverages noise-resilient features inherent in the generative process to extract robust features from noisy images without requiring auxiliary information.

Extensive experiments have been performed to demonstrate the performance gain over the existing state-of-the-art methods.

## 2. Related work

Due to the diversity of modalities in medical imaging, domain adaptation is an important research area in medical imaging. It covers a range of applications, including segmentation (Perone *et al.*, 2019; Liu *et al.*, 2021a; Dong *et al.*, 2020; Wu and Zhuang, 2021; Zhao *et al.*, 2022b), diagnosis (Zhang *et al.*, 2020; Liu *et al.*, 2021b; Du *et al.*, 2023), and lesion detection (Wang *et al.*, 2021; Yang *et al.*, 2020). Compared to supervised domain adaptation, unsupervised domain adaptation without any labels is more challenging. From the perspective of migration objectives, Unsupervised domain adaptation can be divided into two main categories: feature-level domain adaptation (Dou *et al.*, 2019, 2018; Tzeng *et al.*, 2017; Ganin *et al.*, 2016; Vu *et al.*, 2019; Wang *et al.*, 2019) and image-level domain adaptation (Isola *et al.*, 2017; Zhu *et al.*, 2017; Park *et al.*, 2020; Xie *et al.*, 2020; Jeon *et al.*, 2021; Ho *et al.*, 2020; Sasaki *et al.*, 2021; Zhao *et al.*, 2022a; Kim *et al.*, 2023; Mahmood *et al.*, 2018; Mathew *et al.*, 2020, 2022).

### 2.1. Unsupervised domain adaptation in the feature level

The key to feature-level domain adaptation lies in extracting domain-invariant features. Existing work encodes both source and target data into a latent space to extract stable, domain-invariant features. Some methods employed discriminators to differentiate features from the source and target domains, guiding encoders to extract domain-invariant features (Tzeng *et al.*, 2017; Ganin *et al.*, 2016). However, other studies (Vu *et al.*, 2019; Wang *et al.*, 2019) have found that semantic feature maps

and semantic prediction entropy maps are more effective for bridging the gap between source and target domains. Additionally, novel regularization losses have been introduced in domain adaptation tasks. For instance, (Luo *et al.*, 2019; Lee *et al.*, 2019) proposed new metrics to measure discrepancies across datasets. Building on the adversarial training framework, (Tsai *et al.*, 2018) focused on multi-scale feature maps, aligning them at different levels in the semantic feature map space.

Although feature-level domain adaptation is efficient, it mainly targets specific applications, such as segmentation or detection. In contrast, the work presented in this paper focuses on image translation, a more general approach.

### 2.2. Unsupervised domain adaptation in the image level

Image translation involves transforming an input image from one domain to another, with the goal of learning a mapping between two distinct visual domains. As a pioneering work, pix2pix (Isola *et al.*, 2017) introduced a paired image translation method to transfer images from the source domain to the target domain. However, due to the scarcity of paired data, CycleGAN (Zhu *et al.*, 2017) enabled unpaired image translation using cycle-consistency. While CycleGAN-based methods have shown great promise, they often suffer from content distortion. To overcome this limitation, CUT (Park *et al.*, 2020) introduced a contrastive learning strategy, replacing the cycle-consistency constraint and achieving high-quality, one-sided image translation. Similarly, MI2GAN (Xie *et al.*, 2020) addressed the content distortion issue by proposing a disentangling strategy that preserves content information while translating texture. Building on this, IB-GAN (Jeon *et al.*, 2021) was developed, allowing for a trainable latent distribution through the use of a latent encoder.

With the rapid development of diffusion-based models, image translation methods based on diffusion network has become viable alternative to GAN. The Denoising Diffusion Probabilistic Model (DDPM) (Ho *et al.*, 2020) demonstrated its capability to progressively transform Gaussian noise into coherent signals. Subsequent investigations have further explored into the image translation task. UNIT-DDPM (Sasaki *et al.*, 2021) generated target domain images through a denoising Markov Chain Monte Carlo approach conditioned on the source images. EGSDE (Zhao *et al.*, 2022a) trained an assist function on both source and target domains and used it to assist energy-guided stochastic differential equations for realistic image generation. UNSB (Kim *et al.*, 2023) improved the simple Gaussian prior assumption by modeling a sequence of adversarial learning problems, achieving remarkable performance.

In endoscopic navigation, image translation is crucial. (Mahmood *et al.*, 2018) initiated the translation of real images into the virtual domain to enhance sparse medical datasets. Building on this, (Mathew *et al.*, 2020) improved the approach by using cycle consistency loss and incorporating two discriminators to remove specular highlights in the virtual domain. CLTS-GAN (Mathew *et al.*, 2022) further refined techniques for controlling color, lighting, and texture in real endoscopic images, accurately generating illumination information for real-world applications. However, these methods encountered challenges

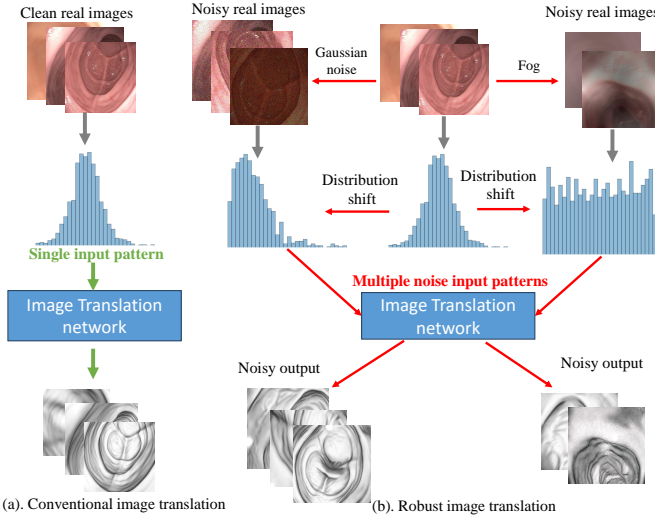


**Fig. 2. Challenges in domain adaptation from real endoscopic image domains to the virtual domain. Image artifacts can lead to biased input distribution and make the image translation network fail.**

with artifacts in endoscopic images. This paper aims to address these issues by proposing a two-stage image translation framework to resolve artifacts in endoscopic image translation.

### 3. Methods

#### 3.1. Problem formulation and motivation

The fundamental principle of image translation is to align the statistical distributions between the source and target domains while preserving the original structures. Although this may appear straightforward, as illustrated in Figure 2 (a), endoscopic scenarios present complex artifacts that can skew the input domain's distribution. For instance, as shown in Figure 2 (b), surgical smoke reduces overall brightness and contrast, resulting in a smoother distribution, while Gaussian noise introduces random perturbations, making the distribution steeper. These ambiguous input distributions can confuse the generative network, leading to erroneous or suboptimal results like blurriness.

To address this issue, this study focuses on two key aspects: 1) Decoupling the image translation process into two steps: local translation for artifact removal and global translation for overall style transfer. 2) Designing a novel contrastive learning strategy during the translation process to extract noise-resilient features.

#### 3.2. The overall framework

As shown in Figure 3, our proposed method encompasses three distinct domains: the noisy real domain (**N**), the clean real domain (**R**), and the virtual domain (**V**). To achieve alignment between these domains, we employ generative adversarial networks, denoted as  $G_x^i$  ( $i = 1, 2$ ),  $G_y^i$  ( $i = 1, 2$ ),  $D_x^i$  ( $i = 1, 2$ ), and  $D_y^i$  ( $i = 1, 2$ ). Specifically, for an input noisy image  $n \in \mathbf{N}$ ,  $G_x^1$  performs a local translation to map it to the clean real domain. Subsequently,  $G_x^2$  carries out a global translation to generate images in the virtual domain. To ensure cycle consistency,

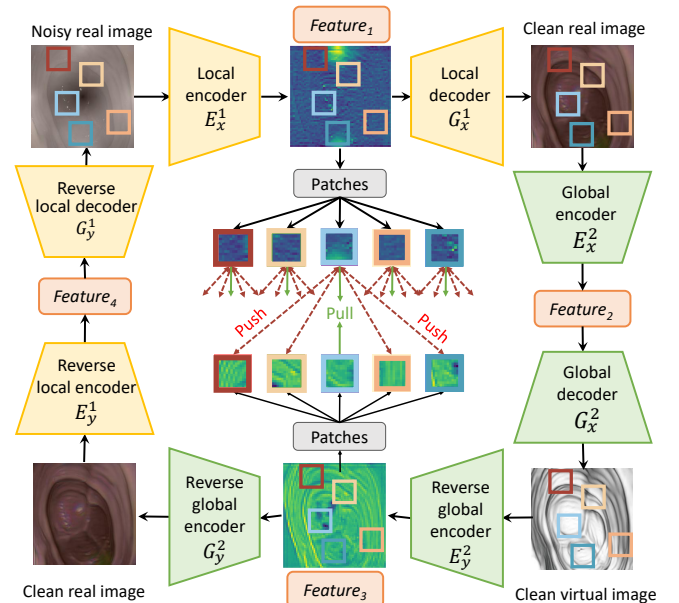


**Fig. 3. Overview of the proposed method for robust image translation from noisy images. Three domains are bridged using four generative networks with cycle consistency. Noise-free features extracted from virtual images guide noisy features extracted from noisy real images using contrastive learning strategy.**

$G_y^1$  and  $G_y^2$  are responsible for generating the corresponding reverse images. The discriminators ( $D_x^i$  and  $D_y^i$ ) aim to accurately classify whether the generated images belong to the target domains, while the generators endeavor to produce images that are indistinguishable from the target domain images. Notably, the feature  $Feature_3$  extracted in encoder  $E_y^2$  are from clean virtual domain, which contains only structural information without any noise. Consequently, a contrastive learning loss is introduced to facilitate the extraction of a noise-resilient feature  $Feature_1$ , using the noise-free feature  $Feature_3$  as a reference.

#### 3.3. Global-local transfer

The presence of complex artifacts results in a distribution shift in real images, which can confuse the conventional methods that rely on a single generative network to address the domain gap. To mitigate this distribution shift, we introduce an intermediate state, the “artifact-free real domain”, and decompose the translation process from noisy real images to clean virtual images into two stages: local translation and global translation. In the local translation step, a local GAN generates artifact-free real images. In the global translation step, a global GAN transfers the overall style from real images to virtual ones.

Due to the lack of artifact-free images in real life clinical settings, we design a pseudo-labels generator based on differential 3D reconstruction and style transfer techniques incorporating statistical objective functions. With the accurate pose ground-truth derived from the virtual domain, this strategy initially establishes a differentiable three-dimensional model for the virtual domain using Gaussian Splatting (Kerbl *et al.*, 2023). Specifically, given the 3D poses ground truth, each Gaussian is

defined by a 3D covariance matrix  $\Sigma$  and a center point  $x$ :

$$G(x) = e^{-\frac{1}{2}x^T \Sigma^{-1} x} \quad (1)$$

where the covariance matrix  $\Sigma$  can be represented by a rotation matrix  $R$  and a scaling matrix  $S$  for differentiable optimization:

$$\Sigma = RSS^T R^T \quad (2)$$

For projecting 3D Gaussian points to 2D images, the rendering process of  $N$  ordered points overlapping a pixel follows a specific formula:

$$C = \sum_{i \in N} c_i \alpha_i \prod_{j=1}^{i-1} (1 - \alpha_j) \quad (3)$$

where  $c_i, \alpha_i$  indicates the color and density of a given point. These parameters are determined by a Gaussian with a covariance matrix  $\Sigma$ , which is then scaled by optimizable per-point opacity and spherical harmonics color coefficients. Formally, the whole virtual structure can be represented by a group parameters of 3D Gaussian model, denoted by  $\Theta$ , where each  $\Theta_i = \{x_i, s_i, q_i, \alpha_i, c_i\}$ , where  $x \in \mathbb{R}^3$  is the position,  $s \in \mathbb{R}^3$  is the scaling factor,  $q \in \mathbb{R}^4$  is the rotation quaternion,  $\alpha \in \mathbb{R}$  is the opacity, and  $c \in \mathbb{R}^k$  is the spherical harmonics coefficients.

Subsequently, to preserve the original virtual structure while transferring the virtual texture to a noise-free real-life texture, we finetune only the spherical harmonics coefficients, while keeping all other parameters fixed. Additionally, two Inception loss functions are introduced, which focus on global feature maps rather than pixel-level features, enabling the generation of real images without pixel-level artifacts.

Formally, for the generated realistic image  $I_g$  and virtual image  $I_v$ ,  $L_{content}$  encourages  $I_g$  and  $I_v$  to have similar content features:

$$L_{content} = \|\tau(I_g) - \tau(I_v)\|_2 \quad (4)$$

where  $\tau()$  is the feature representation obtained from the *relu4\_1* layer of a pretrained VGG-19 network (Simonyan and Zisserman, 2014). In addition, the style loss  $L_{style}$  encourages the feature statistics distance between generated image  $I_g$  and real image  $I_n$  to be small:

$$L_{style} = \sum_l \|\mu(\tau_l(I_g)) - \mu(\tau_l(I_n))\|_2 + \sum_l \|\Sigma(\tau_l(I_g)) - \Sigma(\tau_l(I_n))\|_2 \quad (5)$$

where  $\mu$  and  $\Sigma$  represent the mean and standard deviation respectively, and  $\tau_l()$  denotes the feature representation obtained from the  $l$ -th layer of VGG-19. Since the objective function focuses on feature characteristic rather than pixel characteristic, this method effectively generates realistic images while suppressing artifacts.

After getting the pseudo-labels, the loss function of the local and the global translation steps are designed as follows: we assume the aim is generating target images  $t \in \mathbf{T}$  from source images  $s \in \mathbf{S}$ , then the GAN objective function is:

$$L_{GAN}(S, T, D, G) = \mathbb{E}_{s \sim S} [\log(1 - D(G(s)))] + \mathbb{E}_{t \sim T} [\log D(t)] \quad (6)$$

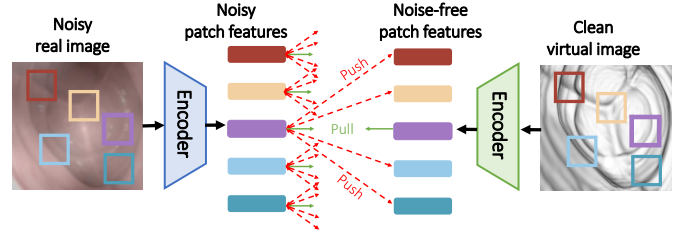


Fig. 4. Noise-resilient feature extraction process. Patch features are extracted by the encoder and the contrastive loss encourages the consistency between noisy features and noise-free features.

For the cycle consistency, images in source domain  $\mathbf{S}$  can be reversed by  $G_{T \rightarrow S}$ , constraining by above objective function  $\min_{G_{T \rightarrow S}} \max_{D_{T \rightarrow S}} L_{GAN}(T, S, D_{T \rightarrow S}, G_{T \rightarrow S})$  and the consistency loss:

$$L_{cyc}(G_{T \rightarrow S}, G_{S \rightarrow T}) = \mathbb{E}_{s \sim S} [\|G_{T \rightarrow S}(G_{S \rightarrow T}(s)) - s\|] + \mathbb{E}_{t \sim T} [\|G_{S \rightarrow T}(G_{T \rightarrow S}(t)) - t\|] \quad (7)$$

Specifically, the local GAN including  $G_x^1, G_y^1, D_x^1, D_y^1$  generates real images without artifacts  $r \in R$  from noisy input  $n \in N$ , and the global GAN  $G_x^2, G_y^2, D_x^2, D_y^2$  generates virtual images  $v \in V$  from  $r \in R$ . Therefore, the full objective function of the local translation and the global translation can be represented as:

$$L_{local} = L_{GAN}(N, R, D_x^1, G_x^1) + L_{GAN}(R, N, D_y^1, G_y^1) + L_{cyc}(G_x^1, G_y^1) \\ L_{global} = L_{GAN}(V, R, D_x^2, G_x^2) + L_{GAN}(R, V, D_y^2, G_y^2) + L_{cyc}(G_x^2, G_y^2) \quad (8)$$

### 3.4. Noise-resilient feature extraction

Although decoupling image translation into global and local steps can enhance the robustness of image translation, a fundamental difficulty persists: artifact features in noisy images lead to suboptimal results. In this section, we propose a novel contrastive learning framework to extract noise-resilient features without any additional auxiliary information.

The introduction of the ‘‘artifact-free real domain’’ in our work enables both noisy and virtual images to be transferred to the same real images using respective GAN networks. Moreover, the translation path from the virtual to the real domain involves global translation without artifacts, ensuring that features extracted from virtual images retain stable structural information. Building on this, we propose a contrastive learning strategy that leverages the inherent noise-free features of virtual images to extract noise-resilient features from noisy input images.

Specifically, for the noisy input images  $n \in N$ , and corresponding generated virtual images  $v \in V$ , the process begins by randomly extracting  $M$  patches from both images, as shown in Figure 4. Next, features are extracted using respective encoder backbones. Since the patch positions are identical in both images, the structural and semantic information should remain

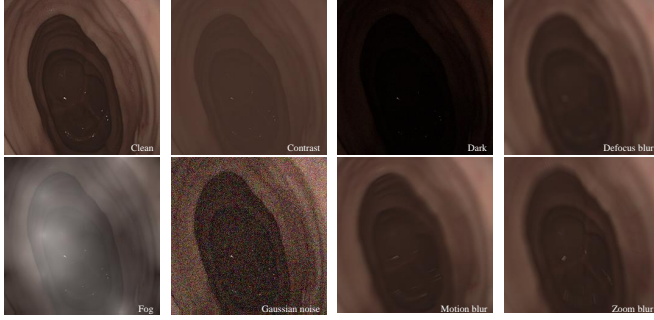


**Fig. 5.** Examples of noisy images generated from C3VD dataset. Seven image corruptions are added to images

consistent. Therefore, any given noisy patch feature should exhibit similarity to its corresponding virtual patch feature, while differing from patch features at other positions.

Formally, for any given patch feature  $q \in \mathbb{R}^k$  in noisy images, it should be similar to the patch feature  $k_+ \in \mathbb{R}^k$  located in the same position in the corresponding virtual image, while being dissimilar to patch features  $k_i \in \mathbb{R}^k$  ( $i=0,1,\dots,M$ ) from other positions in noisy images. Therefore, the proposed objective function is:

$$L_{resilient}(q, k_+, \{k_i\}_{i=1,2,\dots,M}) = -\log \frac{\exp(q \cdot k_+ / \tau)}{\exp(q \cdot k_+ / \tau) + \sum_{i=1}^M \exp(q \cdot k_i / \tau)} \quad (9)$$

For  $P$  query patches in a noisy image, the whole contrastive loss function is  $\sum_{j=1}^P L_{resilient}(q^j, k_+, \{k_i^j\}_{i=1,2,\dots,M})$ . This loss encourages the model to align features from noisy images with their noise-free counterparts in the virtual domain.

## 4. Experiment Settings

### 4.1. Datasets

Detailed experimental validation has been performed on four datasets with different types of artifacts. Specifically, these datasets can be divided into two categories based on the generation process of noise. The first category consists of synthetic noise generated through image corruptions, while the second category comprises *in vivo* noise present in clinical data.

**Synthetic noise datasets:** For images with synthetic noises, we used C3VD dataset (Bobrow *et al.*, 2023), EndoSLAM-Unity dataset (Ozyoruk *et al.*, 2021), and an in-house lung-unity dataset. C3VD contains 22 small colonoscopic video sequences, each paired by corresponding virtual models. Virtual images are extracted from the virtual 3D models in our experiments. EndoSLAM-Unity provides the Unity environment with different virtual and real textures. We sampled 5868 images in colon subset and split them into 10 videos for training and validation. Lung-Unity is an in-house dataset collected from animal experiments. Before the experiments, a whole-body CT scan was performed to reconstruct the pig’s airway model. This model was imported into Unity, where virtual and real images were rendered using corresponding textures, following the same

process as the EndoSLAM-Unity dataset. A total of 19582 images were collected, with 7000 used for training, 7000 for validation, and 5582 for testing. For noise generation, we followed the approach from ImageNet-C (Hendrycks and Dietterich, 2019), applying seven common image corruptions—darkness, zoom blur, defocus blur, contrast reduction, motion blur, fog, and Gaussian noise—to each image in these datasets, as shown in Figure 5. To simulate multiple types of artifacts seen in real surgical scenes, we randomly selected two types of corruptions for each image and superimposed them with varying intensities. Additionally, in Unity, we varied the intensity of illumination to simulate the intense lighting variations commonly encountered in real surgical environments.

**In vivo patient datasets:** *In vivo* datasets were collected during a clinical study involving 25 patients using an endobronchial surgical robot (Precision Robotics, Hong Kong). The study was conducted at Shanghai Chest Hospital with ethical approvals (No. KS23032). All procedures were performed in accordance with ethical standards. Both *In vivo* images and their corresponding virtual images were acquired using a robotics platform. For the virtual images, we imported segmented bronchial trees from pre-operative CT scans into Unity and rendered the virtual images. For the *In vivo* images, we captured videos during the clinical trials with a bronchoscope operating at 25 frames per second (fps). In total, 25 sequences with total 110562 frames are included in our experiments, where 15 sequences for training, 5 sequences for validation, and 5 sequences for testing.

### 4.2. Baselines and metrics

**Quantitative metric:** For quantitative performance evaluation, we evaluate two types of metrics: direct metrics for unpaired image translation tasks and indirect metrics for depth estimation and image registration.

For direct evaluation, we employed traditional unpaired image translation metrics, including Fréchet Inception Distance (FID) (Heusel *et al.*, 2017) and Kernel Inception Distance (KID) (Bińkowski *et al.*, 2018). We additionally measured Structural Similarity Index (SSIM) and Peak Signal-to-Noise Ratio (PSNR) for datasets with available paired test sets (C3VD, EndoSLAM-Unity, and Lung-Unity). For indirect evaluation, we used depth estimation and image registration as auxiliary tasks. In the depth estimation task, a network pre-trained on the virtual domain was used to compute depth maps of images translated from noisy to virtual domains. The evaluation metrics for this task included absolute relative error (Abs Rel), squared relative error (Sq Rel), and root-mean-squared error (RMSE). In the image registration task, each noisy image was translated into the virtual domain, and features were extracted using a pretrained R2Former network (Zhu *et al.*, 2023). We then searched for matching images in the virtual database. If the retrieved results corresponded to the same location as the input image, the localization was considered correct. Specifically, we used a 5-millimeter threshold for correct localization and reported recall as the evaluation metric.

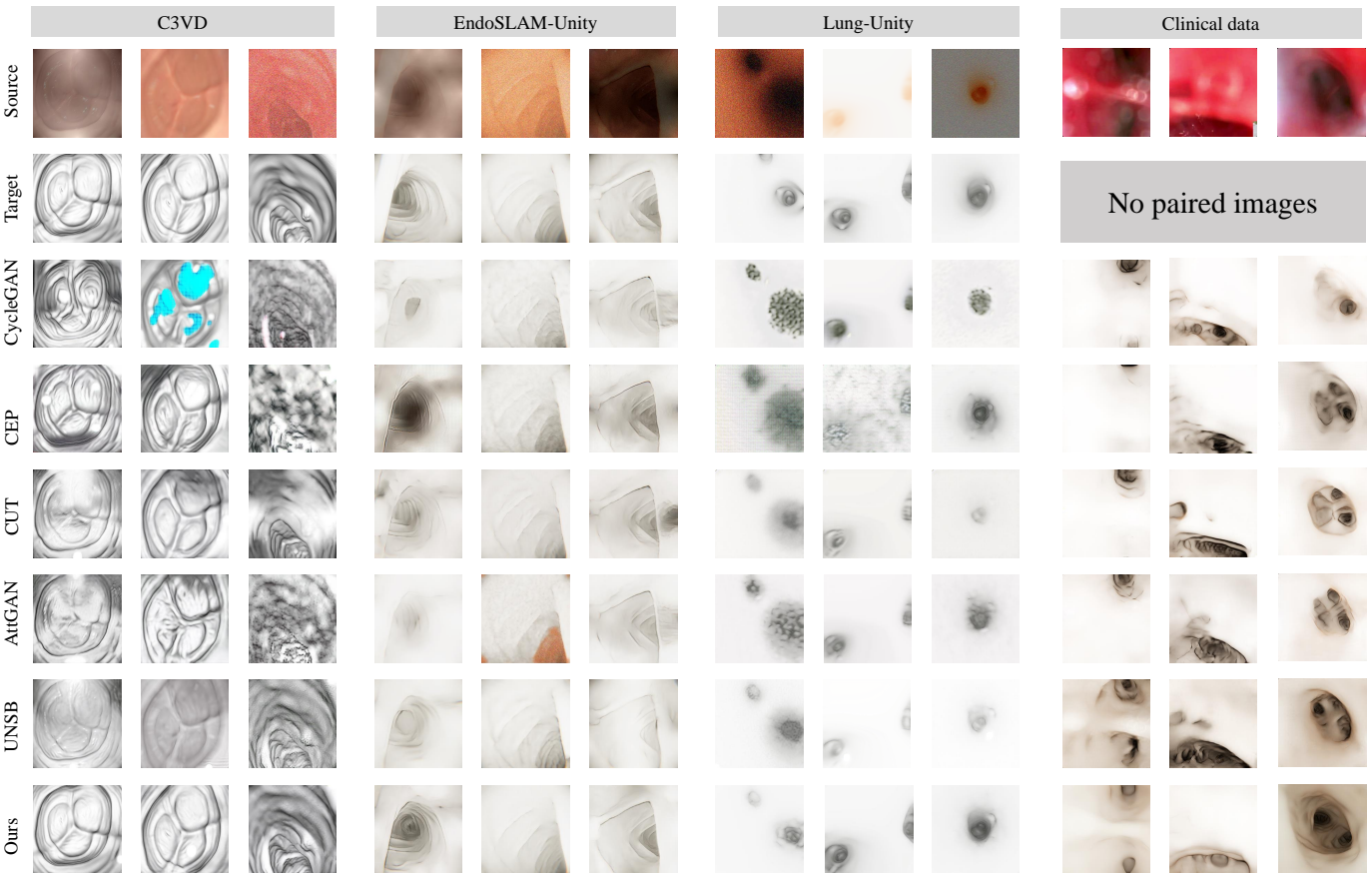
**Baselines of image translation:** Our proposed framework is compared with existing image translation methods including: CycleGAN, CUT, AttentionGAN, CEP, UNSB, Cyclelegan,

**Table 1. Quantitative results of image translation. The best results are in bold.**

	C3VD				EndoSLAM-Unity				LUNG-Unity				Clinical data	
	FID	KID	SSIM	PSNR	FID	KID	SSIM	PSNR	FID	KID	SSIM	PSNR	FID	KID
CycleGAN	130.426	0.101	0.486	28.578	90.612	0.054	0.820	31.030	188.537	0.177	0.883	31.318	206.550	0.171
CUT	117.591	0.131	0.496	28.490	76.315	0.041	0.825	30.018	101.468	0.073	0.910	30.886	183.028	0.150
AttentionGAN	308.010	0.305	0.411	28.131	155.607	0.112	0.823	29.726	186.885	0.172	0.885	32.384	201.289	0.162
CEP	168.518	0.141	0.452	28.405	120.564	0.073	0.772	31.479	147.552	0.114	0.527	31.341	179.064	0.143
UNSB	84.643	0.039	0.544	28.851	78.120	0.041	0.821	31.073	67.563	0.053	0.908	32.768	168.637	0.139
Ours	<b>76.974</b>	<b>0.038</b>	<b>0.570</b>	<b>29.048</b>	<b>68.791</b>	<b>0.038</b>	<b>0.824</b>	<b>31.668</b>	<b>27.082</b>	<b>0.010</b>	<b>0.910</b>	<b>33.671</b>	<b>141.983</b>	<b>0.118</b>

**Table 2. Quantitative results of depth estimation. The best results are in bold.**

	C3VD			EndoSLAM-Unity			LUNG-Unity			Abs_Rel	Sq_Rel	RMSE
	Abs_Rel	Sq_Rel	RMSE	Abs_Rel	Sq_Rel	RMSE	Abs_Rel	Sq_Rel	RMSE			
CycleGAN	0.260±0.103	8.934±7.713	23.472±9.412	0.169±0.101	0.421±0.580	1.708±1.094	0.217±0.130	0.459±0.612	2.053±1.309			
CUT	0.243±0.114	9.026±8.654	23.611±11.463	0.168±0.095	0.421±0.589	1.755±1.132	0.214±0.127	0.446±0.605	1.998±1.267			
AttentionGAN	0.240±0.120	8.602±9.021	22.860±11.440	0.232±0.099	0.654±0.661	2.059±1.168	0.260±0.143	0.501±0.639	2.581±1.730			
CEP	0.241±0.118	8.723±8.857	23.094±11.554	0.171±0.109	0.446±0.660	1.698±1.141	0.210±0.119	0.447±0.598	1.990±1.214			
UNSB	0.303±0.141	12.962±11.388	28.294±13.309	0.152±0.096	0.351±0.512	1.604±1.007	0.196±0.101	0.412±0.530	1.635±0.997			
Ours	<b>0.216±0.102</b>	<b>6.709±7.003</b>	<b>20.088±9.788</b>	<b>0.147±0.084</b>	<b>0.337±0.484</b>	<b>1.533±1.005</b>	<b>0.164±0.091</b>	<b>0.389±0.490</b>	<b>1.371±0.705</b>			

**Fig. 6. Examples of the source domain, target domain, and the results of transferring from the source to the target. It is evident that our method effectively mitigates the effect of noise, successfully transforming a noisy image into a virtual image.**

CUT, AttentionGAN and CEP employed generative adversarial network to transfer the source domain to the target domain, while UNSB used diffusion-based network to generate target-like images.

## 5. Image translation results

In this section, we compared the proposed framework with SoTA baselines for image translation.

### 5.1. Results for synthetic noise

Table 1 shows the quantitative comparison. It is evident that our framework outperforms other methods significantly in all

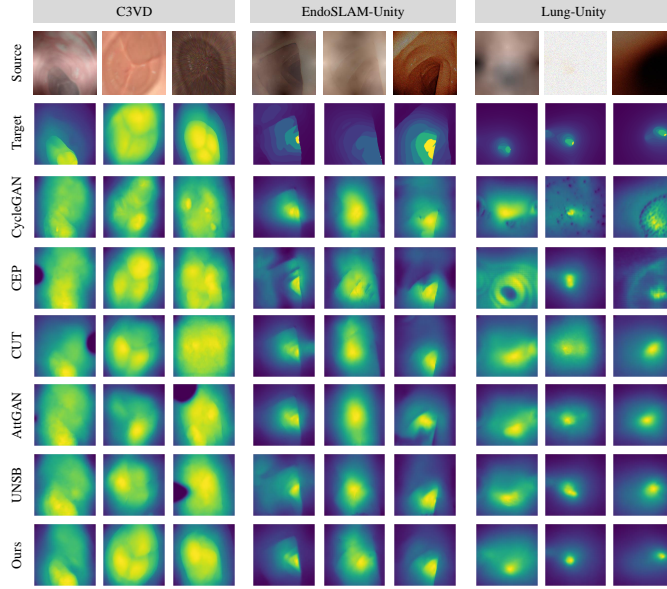


**Fig. 7.** Examples of the source image, depth ground truth, and the results of depth estimation evaluating on the transferred images using different methods.

**Table 3. Quantitative results of image registration. The best results are in bold.**

	C3VD	EndoSLAM-Unity	Lung-Unity	Clinical data
CycleGAN	47.8	56.2	13.0	46.1
CUT	39.3	72.1	10.7	54.0
AttentionGAN	17.0	28.2	17.7	48.3
CEP	38.3	55.8	18.2	60.7
UNSB	56.5	71.1	19.8	63.9
<b>Ours</b>	<b>62.3</b>	<b>82.6</b>	<b>44.7</b>	<b>71.6</b>

metrics. Even comparing with the SoTA diffusion-based model UNSB, our method achieved an average improvement of 0.56 dB in PSNR. In addition, the t-test were conducted to compare different methods. The p-values for PSNR between our method and UNSB are 7.5e-12, 0.094, 1.05e-74 across three datasets, suggesting that the improvements are statistically significant.

Detailed qualitative results are demonstrated in Figure 6. The strong noise in real images lead to input distribution shift and noisy features, thereby hindering the translation into a clean virtual domain with GAN-based methods. For example, in the first column of the Lung-Unity dataset, when confronted with Gaussian noise, all GAN-based methods generated virtual images with grainy structures. Diffusion-based approaches, such as UNSB, initially applied Gaussian noise to the input image during training, which helped mitigate local artifacts to some extent. However, for global artifacts like fog, it produced blurred outputs, as seen in the first column of the C3VD dataset. In contrast, our method generated clean virtual images similar to the target domain, since two separate generative networks (local GAN and global GAN) have distinct roles and do not interfere with each other, and extracted noise-resilient features from noisy images.

## 5.2. Results for *in vivo* clinical data

To validate the robustness of image translation method in clinical scenarios, we conducted experiments using clinical scenes containing complex artifacts. Due to tissue deformations, the images in real scene cannot match perfectly with corresponding virtual images. Therefore, we discarded pixel-level metrics and only evaluated the FID and KID.

The results are shown in Table 1. It is evident that with the proposed strategy, FID and KID improved by a large margin. Figure 6 visualized the generation results of different methods under real artifacts. It demonstrated that conventional methods faced two challenges: overfitting to artifact features and failing to preserve the original structure. For example, in the third column of the clinical dataset, the presence of mucus artifacts caused conventional methods to generate an image with four lumens, which did not match the anatomical structure. In contrast, our method successfully produced the correct structure with two lumens.

## 6. Applications to downstream tasks

### 6.1. Depth estimation

Detailed experiments were conducted on the depth estimation task. The results, shown in Table 2, demonstrate that our method outperforms all baseline methods on all indirect metrics. This superior performance can be attributed to the method’s ability to generate virtual images that closely resemble the virtual domain. Figure 7 visualizes the estimated depth, further illustrating that the baseline methods failed to accurately estimate depth due to the presence of strong artifacts. For example, in the third column of the C3VD dataset, conventional methods produce either black regions (AttGAN, UNSB) or blurred results (CycleGAN, CUT, CEP). In contrast, our method achieves precise depth estimation, thanks to its robustness in image translation.

### 6.2. Image registration

In this section, we demonstrate that the proposed image translation method can be applied to endoscopic navigation. This is achieved by co-registering real-time 2D endoscopic videos with virtual databases, which can be formulated as an image registration task. Figure 8 and Table 3 show the image registration results using R2former (Zhu *et al.*, 2023) as the backbone. Due to the presence of artifacts in real images, conventional methods either overfit to artifact features (CEP, UNSB) or generate blurred images (CycleGAN, CUT, AttGAN), making it difficult to match corresponding images from virtual databases. In contrast, our method generates clean virtual images, leading to the highest recall rate in the image registration process.

### 6.3. Zero-shot results to real-world scenario

In this section, we investigate the generalizability of image translation methods. To this end, we trained image translation networks using the EndoSLAM Unity dataset and evaluated their performance on the Endoscopy Artifact Detection

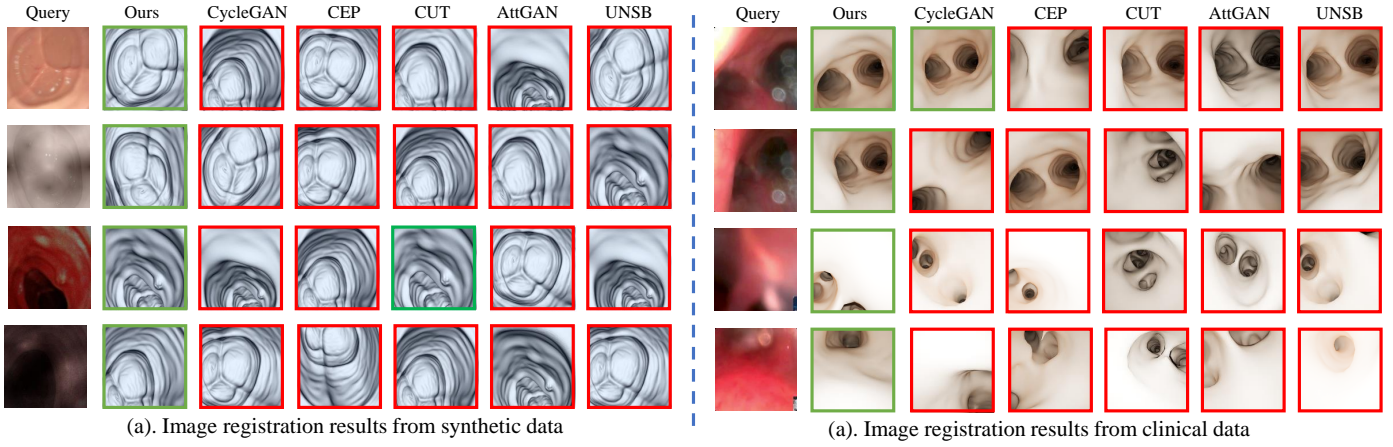


**Fig. 8. Visualization results of image registration.** Owing to the noise-resilient image translation capability, the proposed method successfully matches the right virtual images, while other methods return incorrect images.

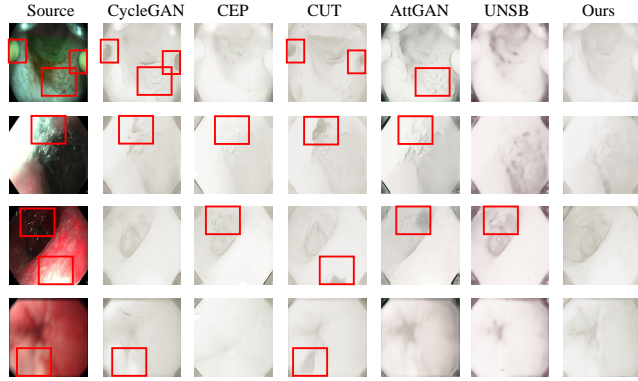


**Fig. 9. Zero-shot results on EAD dataset.** Red boxes represent artifact areas.

(EAD) dataset (Ali *et al.*, 2019), which includes diverse artifacts encountered in real-world scenarios, such as bubbles, blur, and specularity. As illustrated in Figure 9, the presence of complex textures and various artifacts posed significant challenges for image translation methods. Conventional methods often focused on artifact features when translating to the virtual domain, as highlighted by the red boxes in Figure 9. Moreover, in the presence of image blurriness, as seen in the last row, some methods (CEP, UNSB) failed to accurately estimate structural information. In contrast, our proposed method, which employs a decoupling strategy and extracts inherent noise-resilient features, effectively mitigated artifacts while preserving structural information. This demonstrates its superior capability in handling a wide range of artifacts.

## 7. Discussion

### 7.1. Ablation study

Ablation studies were performed to investigate the relative contributions of the proposed components to the final results. The key components of our strategy consist of two parts: decoupling the image translation task to the local step and the global

**Table 4. Ablation on each component.** We use CUT as baseline model and evaluate on C3VD dataset. We find that each component plays a critical role.

	Component	FID	KID
“Decoupling” strategy	“Resilient feature extraction” strategy		
✗	✗	183.028	0.150
✓	✗	169.321	0.134
✓	✓	<b>141.983</b>	<b>0.118</b>

step, and an inherent noise-resilient feature extraction strategy. To investigate the impact of each component on the robust image translation, we conducted an ablation study and the results are presented in Table 4. It is evident that the baseline method, CUT without any of our contributions, exhibits suboptimal performance. However, the incorporation of “decoupling” strategy, as well as the inherent noise-resilient feature extraction strategy, lead to noticeable improvements in performance.

### 7.2. The bottleneck of image translation from noisy images

It is intriguing to explore why traditional image translation methods struggle with artifacts. In this section, we investigate this issue from a feature-level perspective. We posit that artifacts in extracted features significantly impact the image translation process.

To verify this claim, we first visualize the feature maps extracted from both clean images and noisy images. As shown in Figure 10 (a), feature maps extracted from clean images using the CUT model exhibit a smooth appearance and accurately reflect the structure. However, when extracting features from noisy images, different types of noise result in various distortions. For example, Gaussian noise leads to pronounced granular artifacts, while blurring causes significant deviations in the feature maps. In contrast, the feature maps extracted using our proposed method are closer to those from clean images.

Furthermore, we computed the feature map distance between feature maps from the clean images and those from noisy images, and investigated the correlation between the feature map distance and the final PSNR performance. The results, shown in Figures 10 (b), (c), revealed a clear negative correlation be-

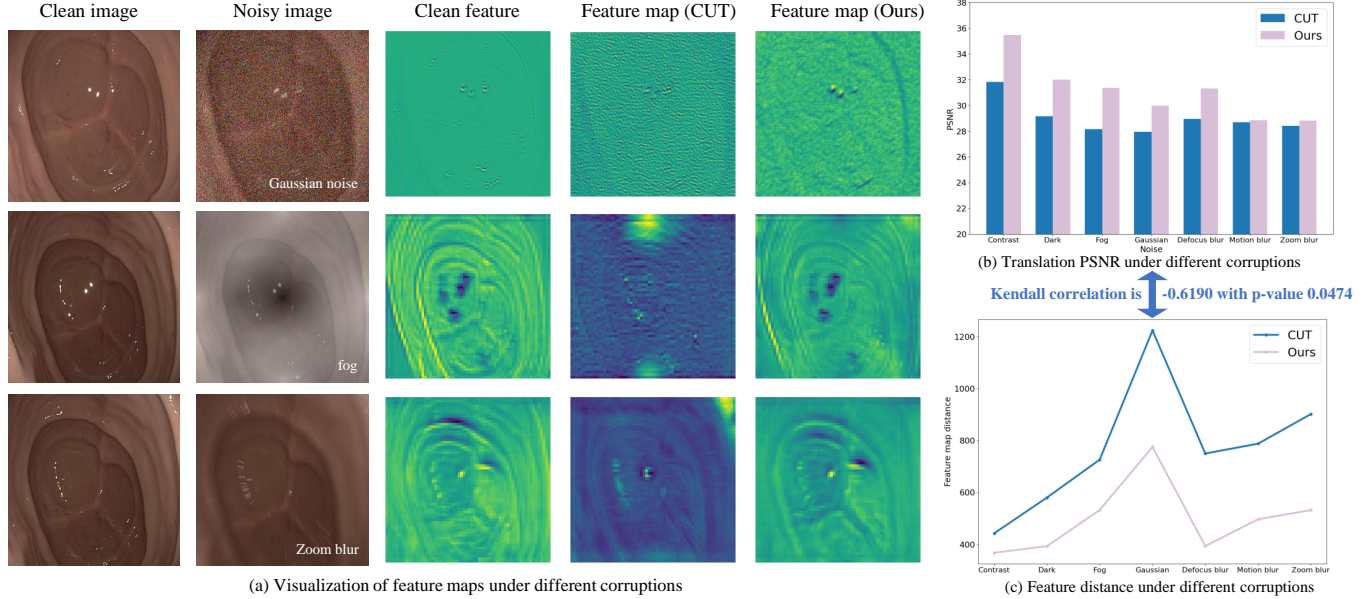


**Fig. 10.** An analysis of the Robust Image Translation Bottleneck. **a.** Visualization of clean image, noisy image and corresponding feature map demonstrates that feature map extracted by our method is more similar to the noise-free features. **b** Feature map distance under different corruptions. **c** PSNR under different corruptions.

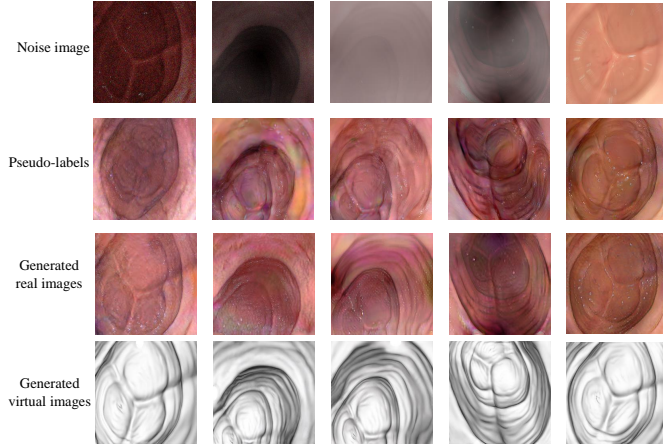


**Fig. 11.** Examples of noise images, pseudo-labels generated by gaussian splatting, the local transfer results, and global transfer results.

tween feature map distance and PSNR. The “contrast” setting, which showed the smallest feature map distance, achieved the highest PSNR, whereas the “Gaussian noise” setting, with the greatest feature map distance, resulted in the lowest PSNR. Furthermore, we calculated the Kendall correlation coefficient between the feature map distance and PSNR, which was -0.6190 with a p-value of 0.0474, indicating a significant negative correlation.

These findings suggest that our proposed strategy, which focuses on extracting inherently noise-resilient features, effectively leverages stable latent features to enhance denoising at the feature level, thereby improving PSNR.

### 7.3. Delving into each translation step

In this section, we discuss the generation details of pseudo-labels in the local translation step and the respective results obtained from the two-step translation process.

As shown in the second row of Figure 11, pseudo-labels are robust against artifacts, due to the stable Gaussian Splatting and global statistical loss functions we designed. Furthermore, the two-stage image translation approach exhibits mutual reinforcement. From the second and third rows in Figure 11, we noted a counterintuitive phenomenon: generated real images from the local translation step are clearer than the pseudo-labels, even though the pseudo-labels are considered as the “ground-truth” in this step. We attribute this to the fact that the generated real images are also used as input for the global translation stage. Since the ultimate goal is to produce optimal virtual images, the generated real images can be further optimized during the global translation. Consequently, the local and global steps mutually enhance each other throughout the two-stage training process.

## 8. Conclusion

In this paper, we introduce a novel approach to robust image translation in the presence of artifacts. We have investigated whether image translation networks can effectively transform images with artifacts into the virtual domain. To this end, we have developed a benchmark comprising seven types of synthetic noise and *in vivo* artifacts commonly encountered in endoscopic scenarios. In-depth analyses were performed to assess the bottlenecks that can cause the conventional methods to fail. Building on these insights, we proposed a robust image translation network with two steps: a local step for denoising input images, and a global step for style transfer. Additionally,

we introduced a novel contrastive strategy that leverages the noise-free features inherent in the GAN networks as a reference for guiding the denoising process in noisy images. Experimental results on both public datasets and in-house patient studies demonstrated much improved performance compared of that of the current state-of-the-art. The resilience to complex artifacts notably enhances the robustness of image translation, benefiting downstream tasks such as depth estimation and image registration.

## References

Ali, S., Zhou, F., Daul, C., Braden, B., Bailey, A., Realdon, S., East, J., Wagnier, G., Loschenov, V., Grisan, E., et al., 2019. Endoscopy artifact detection (ead 2019) challenge dataset. *arXiv preprint arXiv:1905.03209* .

Bińkowski, M., Sutherland, D.J., Arbel, M., Gretton, A., 2018. Demystifying mmd gans. *arXiv preprint arXiv:1801.01401* .

Bobrow, T.L., Golhar, M., Vijayan, R., Akshintala, V.S., Garcia, J.R., Durr, N.J., 2023. Colonoscopy 3d video dataset with paired depth from 2d-3d registration. *Medical image analysis* 90, 102956.

Dong, J., Cong, Y., Sun, G., Zhong, B., Xu, X., 2020. What can be transferred: Unsupervised domain adaptation for endoscopic lesions segmentation, in: *Proceedings of the IEEE/CVF conference on computer vision and pattern recognition*, pp. 4023–4032.

Dou, Q., Ouyang, C., Chen, C., Chen, H., Glocker, B., Zhuang, X., Heng, P.A., 2019. Pnp-adanet: Plug-and-play adversarial domain adaptation network at unpaired cross-modality cardiac segmentation. *IEEE Access* 7, 99065–99076.

Dou, Q., Ouyang, C., Chen, C., Chen, H., Heng, P.A., 2018. Unsupervised cross-modality domain adaptation of convnets for biomedical image segmentations with adversarial loss. *arXiv preprint arXiv:1804.10916* .

Du, M., Yang, Y., Zhang, L., 2023. Diagnosis of atrial fibrillation based on unsupervised domain adaptation. *Computers in Biology and Medicine* 164, 107275.

Ganin, Y., Ustinova, E., Ajakan, H., Germain, P., Larochelle, H., Laviolette, F., March, M., Lempitsky, V., 2016. Domain-adversarial training of neural networks. *Journal of machine learning research* 17, 1–35.

Hendrycks, D., Dietterich, T., 2019. Benchmarking neural network robustness to common corruptions and perturbations. *arXiv preprint arXiv:1903.12261* .

Heusel, M., Ramsauer, H., Unterthiner, T., Nessler, B., Hochreiter, S., 2017. Gans trained by a two time-scale update rule converge to a local nash equilibrium. *Advances in neural information processing systems* 30.

Ho, J., Jain, A., Abbeel, P., 2020. Denoising diffusion probabilistic models. *Advances in neural information processing systems* 33, 6840–6851.

Isola, P., Zhu, J.Y., Zhou, T., Efros, A.A., 2017. Image-to-image translation with conditional adversarial networks, in: *Proceedings of the IEEE conference on computer vision and pattern recognition*, pp. 1125–1134.

Jeon, I., Lee, W., Pyeon, M., Kim, G., 2021. Ib-gan: Disentangled representation learning with information bottleneck generative adversarial networks, in: *Proceedings of the AAAI Conference on Artificial Intelligence*, pp. 7926–7934.

Kerbl, B., Kopanas, G., Leimkühler, T., Drettakis, G., 2023. 3d gaussian splatting for real-time radiance field rendering. *ACM Transactions on Graphics* 42, 1–14.

Kim, B., Kwon, G., Kim, K., Ye, J.C., 2023. Unpaired image-to-image translation via neural schrödinger bridge. *arXiv preprint arXiv:2305.15086* .

Lee, C.Y., Batra, T., Baig, M.H., Ulbricht, D., 2019. Sliced wasserstein discrepancy for unsupervised domain adaptation, in: *Proceedings of the IEEE/CVF conference on computer vision and pattern recognition*, pp. 10285–10295.

Liu, L., Zhang, Z., Li, S., Ma, K., Zheng, Y., 2021a. S-cuda: self-cleansing unsupervised domain adaptation for medical image segmentation. *Medical Image Analysis* 74, 102214.

Liu, X., Liu, X., Hu, B., Ji, W., Xing, F., Lu, J., You, J., Kuo, C.C.J., El Fakhri, G., Woo, J., 2021b. Subtype-aware unsupervised domain adaptation for medical diagnosis, in: *Proceedings of the AAAI conference on artificial intelligence*, pp. 2189–2197.

Luo, Y., Zheng, L., Guan, T., Yu, J., Yang, Y., 2019. Taking a closer look at domain shift: Category-level adversaries for semantics consistent domain adaptation, in: *Proceedings of the IEEE/CVF conference on computer vision and pattern recognition*, pp. 2507–2516.

Mahmood, F., Chen, R., Durr, N.J., 2018. Unsupervised reverse domain adaptation for synthetic medical images via adversarial training. *IEEE transactions on medical imaging* 37, 2572–2581.

Mathew, S., Nadeem, S., Kaufman, A., 2022. Clts-gan: color-lighting-texture-specular reflection augmentation for colonoscopy, in: *International Conference on Medical Image Computing and Computer-Assisted Intervention*, Springer. pp. 519–529.

Mathew, S., Nadeem, S., Kumari, S., Kaufman, A., 2020. Augmenting colonoscopy using extended and directional cyclegan for lossy image translation, in: *Proceedings of the IEEE/CVF Conference on Computer Vision and Pattern Recognition*, pp. 4696–4705.

Ozyoruk, K.B., Gokcelez, G.I., Bobrow, T.L., Coskun, G., Incetan, K., Almalioglu, Y., Mahmood, F., Curto, E., Perdigoto, L., Oliveira, M., et al., 2021. Endoslam dataset and an unsupervised monocular visual odometry and depth estimation approach for endoscopic videos. *Medical image analysis* 71, 102058.

Park, T., Efros, A.A., Zhang, R., Zhu, J.Y., 2020. Contrastive learning for unpaired image-to-image translation, in: *Computer Vision–ECCV 2020: 16th European Conference, Glasgow, UK, August 23–28, 2020, Proceedings, Part IX 16*, Springer. pp. 319–345.

Perone, C.S., Ballester, P., Barros, R.C., Cohen-Adad, J., 2019. Unsupervised domain adaptation for medical imaging segmentation with self-ensembling. *NeuroImage* 194, 1–11.

Razavi, A., Van den Oord, A., Vinyals, O., 2019. Generating diverse high-fidelity images with vq-vae-2. *Advances in neural information processing systems* 32.

Sasaki, H., Willcocks, C.G., Breckon, T.P., 2021. Unit-ddpm: Unpaired image translation with denoising diffusion probabilistic models. *arXiv preprint arXiv:2104.05358* .

Simonyan, K., Zisserman, A., 2014. Very deep convolutional networks for large-scale image recognition. *arXiv preprint arXiv:1409.1556* .

Tang, H., Liu, H., Xu, D., Torr, P.H., Sebe, N., 2021. Attentiongan: Unpaired image-to-image translation using attention-guided generative adversarial networks. *IEEE transactions on neural networks and learning systems* 34, 1972–1987.

Tiwary, P., Bhattacharyya, K., Prathosh, A., 2024. Cycle consistent twin energy-based models for image-to-image translation. *Medical Image Analysis* 91, 103031.

Tsai, Y.H., Hung, W.C., Schulter, S., Sohn, K., Yang, M.H., Chandraker, M., 2018. Learning to adapt structured output space for semantic segmentation, in: *Proceedings of the IEEE conference on computer vision and pattern recognition*, pp. 7472–7481.

Tzeng, E., Hoffman, J., Saenko, K., Darrell, T., 2017. Adversarial discriminative domain adaptation, in: *Proceedings of the IEEE conference on computer vision and pattern recognition*, pp. 7167–7176.

Vu, T.H., Jain, H., Bucher, M., Cord, M., Pérez, P., 2019. Advent: Adversarial entropy minimization for domain adaptation in semantic segmentation, in: *Proceedings of the IEEE/CVF conference on computer vision and pattern recognition*, pp. 2517–2526.

Wang, J., He, Y., Fang, W., Chen, Y., Li, W., Shi, G., 2021. Unsupervised domain adaptation model for lesion detection in retinal oct images. *Physics in Medicine & Biology* 66, 215006.

Wang, S., Yu, L., Li, K., Yang, X., Fu, C.W., Heng, P.A., 2019. Boundary and entropy-driven adversarial learning for fundus image segmentation, in: *Medical Image Computing and Computer Assisted Intervention–MICCAI 2019: 22nd International Conference, Shenzhen, China, October 13–17, 2019, Proceedings, Part I 22*, Springer. pp. 102–110.

Wu, F., Zhuang, X., 2021. Unsupervised domain adaptation with variational approximation for cardiac segmentation. *IEEE Transactions on Medical Imaging* 40, 3555–3567.

Xie, X., Chen, J., Li, Y., Shen, L., Ma, K., Zheng, Y., 2020. Mi 2 gan: generative adversarial network for medical image domain adaptation using mutual information constraint, in: *International Conference on Medical Image Computing and Computer-Assisted Intervention*, Springer. pp. 516–525.

Yang, S., Zhou, X., Wang, J., Xie, G., Lv, C., Gao, P., Lv, B., 2020. Unsupervised domain adaptation for cross-device oct lesion detection via learning adaptive features, in: *2020 IEEE 17th international symposium on biomedical imaging (ISBI)*, IEEE. pp. 1570–1573.

Zhang, Y., Wei, Y., Wu, Q., Zhao, P., Niu, S., Huang, J., Tan, M., 2020. Collaborative unsupervised domain adaptation for medical image diagnosis. *IEEE*

Transactions on Image Processing 29, 7834–7844.

Zhao, M., Bao, F., Li, C., Zhu, J., 2022a. Egsde: Unpaired image-to-image translation via energy-guided stochastic differential equations. Advances in Neural Information Processing Systems 35, 3609–3623.

Zhao, Y., Chen, C., 2021. Unpaired image-to-image translation via latent energy transport, in: Proceedings of the IEEE/CVF conference on computer vision and pattern recognition, pp. 16418–16427.

Zhao, Y., Xie, J., Li, P., 2020. Learning energy-based generative models via coarse-to-fine expanding and sampling, in: International Conference on Learning Representations.

Zhao, Z., Zhou, F., Xu, K., Zeng, Z., Guan, C., Zhou, S.K., 2022b. Le-uda: Label-efficient unsupervised domain adaptation for medical image segmentation. IEEE transactions on medical imaging 42, 633–646.

Zhu, J.Y., Park, T., Isola, P., Efros, A.A., 2017. Unpaired image-to-image translation using cycle-consistent adversarial networks, in: Proceedings of the IEEE international conference on computer vision, pp. 2223–2232.

Zhu, S., Yang, L., Chen, C., Shah, M., Shen, X., Wang, H., 2023. R2former: Unified retrieval and reranking transformer for place recognition, in: Proceedings of the IEEE/CVF Conference on Computer Vision and Pattern Recognition, pp. 19370–19380.